PHYSICAL REVIEW B **108**, 075413 (2023)

Large shift currents via in-gap and charge-neutral excitons in a monolayer and nanotubes of BN

Yi-Shiuan Huang[1], Yang-Hao Chan,[2,3,*] and Guang-Yu Guo[1,2,†]
[1]*Department of Physics and Center for Theoretical Physics, National Taiwan University, Taipei 10617, Taiwan*
[2]*Physics Division, National Center for Theoretical Sciences, Taipei 10617, Taiwan*
[3]*Institute of Atomic and Molecular Sciences, Academia Sinica, Taipei 10617, Taiwan*

(Received 15 May 2023; revised 4 July 2023; accepted 27 July 2023; published 14 August 2023)

We perform *ab initio* many-body calculations to investigate the exciton shift current in small-diameter zigzag BN nanotubes and also single BN sheet, using the *GW* plus Bethe-Salpeter equation (*GW*-BSE) method with the newly developed efficient algorithms. Our *GW*-BSE calculations reveal a large in-gap peak in the shift current spectrum in all the studied BN systems due to the *A* exciton. The peak value of the excitonic shift current is more than three times larger than that of the quasiparticle shift current, and is attributed to the significant enhancement of the optical dipole matrix element by the *A* exciton. The effective exciton shift current conductivity is nearly 10 times larger than the largest shift conductivity observed in ferroelectric semiconductors. Importantly, the direction of the shift current in the BN nanotubes is found to be independent of the tube chirality $(n, 0)$ (or diameter), contrary to the simple rule of $\mathrm{sgn}(J_{\mathrm{shift}}) = \mathrm{mod}(n, 3)$ predicted by previous model Hamiltonian studies. Finally, our *ab initio* calculations also show that the exciton excitation energies decrease significantly with the decreasing diameter due to the curvature-induced orbital rehybridization in small-diameter zigzag BN nanotubes.

DOI: 10.1103/PhysRevB.108.075413

I. INTRODUCTION

Shift current is one of the primary mechanisms for the bulk photovoltaic effect (BPVE) (also known as the photogalvanic effect), which can generate DC photocurrent in noncentrosymmetric crystals due to their second-order optical response to light irradiation. The shift of the real-space Wannier charge center of the excited electron is responsible for the shift current [1–4]. In contrast to the conventional photovoltaic effect, shift current is a bulk phenomenon that does not require a *p*-*n* junction to separate the optically generated electron-hole pairs for a DC photocurrent. Consequently, the BPVE can be exploited to generate the above band-gap photovoltage [5] and thus to fabricate high photoconversion efficiency solar cells [6]. Therefore, there has been a resurgence of interest in the BPVE in recent years.

An exciton is a type of collective excitation formed by a bound electron-hole pair interacting via Coulomb interaction, and can be optically generated. Although an exciton itself is charge neutral, the process of exciton excitation can generate a shift current called exciton shift current due to the Wannier charge center shift of the electron and hole in noncentrosymmetric crystals [7]. Furthermore, the exciton shift current can have exotic subband gap peaks owing to the exciton binding energy [7,8]. Recently, the subband gap exciton shift current was observed in the noncentrosymmetric semiconductor CdS by using THz emission spectroscopy at the low temperature of 2 K [9]. The amplitude of the exciton shift current is comparable to the shift current driven by free electron-hole pair excitation.

BN nanotubes (BN-NTs) are formed by rolling up a single hexagonal BN sheet (see Fig. 1) along a specific chiral vector (n, m) [10]. There are three types of BN-NTs, namely, armchair (n, n) nanotubes, zigzag $(n, 0)$ nanotubes (Fig. 1), and chiral (n, m) nanotubes where $n \neq m$ [10]. However, there is no second-order nonlinear optical (NLO) response (e.g., second-harmonic generation and BPVE) in armchair BN-NTs [11]. Moreover, previous experiments [12] indicate that among the grown BN-NTs, the zigzag structure is usually favored. Therefore, we focus on zigzag BN-NTs in this paper.

BN-NTs exhibit large many-body interaction effects owing to their one-dimensional (1D) and wide-band-gap nature, as have been demonstrated by previous *ab initio* many-body theory studies at the level of *GW* plus Bethe-Salpeter equation (*GW*-BSE) [13,14]. Furthermore, large diameter-dependent *A* exciton peaks have been observed in BN-NTs [15,16], being consistent with the theoretical predictions [13,14]. Therefore, we expect zigzag BN-NTs to be ideal candidates for observing the large subband gap exciton shift current due to their following two properties [9]. First, exciton absorption spectra in BN-NTs are well separated from the continuum of free electron-hole excitation owing to their significantly renormalized optical spectra and large exciton binding energy [13,14]. Second, strongly bounded excitons with a large binding energy impede thermal dissociation into free electron-hole pairs [13,14].

However, *ab initio* studies of the BPVE in BN-NTs at *GW*-BSE level have not been reported, mainly because such *ab initio* calculations are technically and computationally challenging, as will be explained below. Nevertheless, simple

---

[*] yanghao@gate.sinica.edu.tw
[†] gyguo@phys.ntu.edu.tw

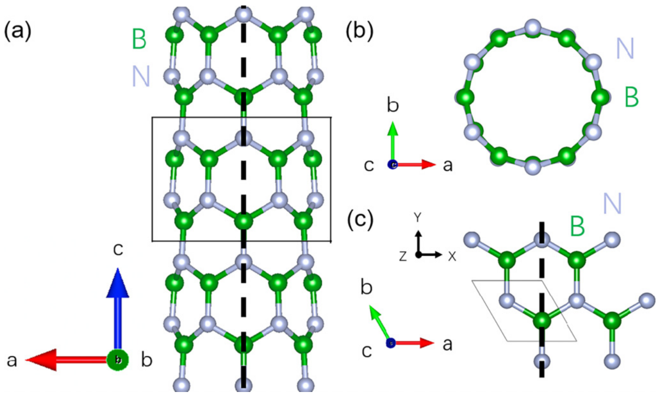

FIG. 1. Crystal structures of the zigzag BN-NT (6,0) and the hexagonal BN sheet. (a) Side and (b) top views of the (6,0) BN-NT. (c) Top view of the single BN sheet. The solid box in (a) indicates the unit cell. Dashed lines in (a) and (c) denote the mirror planes.

model Hamiltonian calculations without [17] and with [18] the inclusion of the the excitonic effect have been performed, predicting that zigzag BN-NTs have shift current along the tube axis with the direction determined by the chiral index (n,0). In particular, the shift current direction would follow the simple rule of sgn($J_{\rm sh}$) = mod(n,3) [17,18]. According to this rule, in a bundle of zigzag BN-NTs, $\frac{1}{3}$ of them would have the shift current along the positive tube axis, another $\frac{1}{3}$ would possess the current flowing in the opposite direction, and the other $\frac{1}{3}$ would have the zero current. That is to say, a bundle of zigzag BN-NTs would have either zero or very small net shift current, i.e., zigzag BN-NTs would not be suitable for applications in photovoltaic solar cells and nonlinear optoelectronic devices. On the other hand, the prediction of this simple rule is theoretically surprising. A symmetry analysis (see Sec. II A below) indicates that the shift current would flow along the y axis in a single BN sheet [see Fig. 1(c)], which is also the tube axis when the BN sheet is rolled up to form a zigzag BN-NT. Consequently, for zigzag BN-NTs with a large diameter, the shift current would always be along the positive tube axis since the curvature effect would be very small [11,19], i.e., the above-mentioned rule would not occur. In this context, it is important to perform the state-of-the-art *ab initio* calculations to investigate this detrimental prediction.

In this work, therefore, we perform the state-of-the-art *ab initio GW*-BSE calculations of the shift current in small-diameter zigzag BN-NTs [(5,0), (6,0), (7,0), (8,0)] as well as single BN layer. Because of possible large curvature effect on the optical properties [11,19], the shift current in small BN-NTs could depend significantly on the tube diameter. On the other hand, the optical properties of large-diameter BN-NTs would be rather similar to that of the single BN sheet [11,19], and thus are not considered here. Among other things, our *ab initio* calculations reveal that the shift current due to the excitons will be large. Furthermore, the direction of the shift current calculated without and with the excitonic effect included is always along the c axis, i.e., being independent on the tube index (n, 0) (or tube diameter). Therefore, our work demonstrates that the zigzag BN-NT bundles are promising materials for high photoconversion efficiency solar cells as well as high-sensitivity photodectors.

We would like to comment that extending the existing *ab initio GW*-BSE approach to calculate the exciton shift current is not straightforward [8]. In fact, there has been only one reported fully *ab initio* study on the exciton shift current [8]. In Ref. [20], to account for the excitonic effect, Fei *et al.* used the linear optical coefficients derived from their *ab initio GW*-BSE calculations. However, since the Coulomb interaction between the electron and hole in an exciton is not explicitly taken into account, such calculations are still based on an independent-particle approximation [20] and hence are not a fully *ab initio GW*-BSE approach. In Ref. [8], to take the strong excitonic effect in two-dimensional (2D) materials into account, a time-dependent adiabatic *GW* (TD-a*GW*) approach was developed and used to calculate the exciton shift current. Although the *ab initio* TD-a*GW* method can properly include the excitonic effect on the optical responses [8], the extremely high computational cost of conducting real-time propagation prevents it from studying complex structures such as BN-NTs. In this work, we thus develop a computationally efficient approach that combines the *GW*-BSE and sum-over-state formalism derived from the perturbative density-matrix approach within the mean-field approximation [21] to calculate the exciton shift current.

The rest of this paper is organized as follows. In Sec. II, we introduce the crystal structure of the BN-NTs and the BN sheet, followed by a brief description of the theories and computational details used in this work. In particular, the computationally efficient approach mentioned above for the exciton shift current calculations will be outlined. The main results are presented in Sec. III. In Sec. III A, we present the calculated electronic and optical properties of the BN sheet. The distinguished features in the optical spectra are analyzed in terms of the electronic band structure and interband optical transition matrix elements. In Sec. III B, the electronic properties of the BN-NTs are reported, which will be used to understand the calculated optical absorption and shift current spectra in subsections that follows. In Secs. III C and III D, the calculated optical absorption and shift current spectra of the BN-NTs are presented, respectively. Finally, the conclusions drawn from this work are summarized in Sec. IV.

II. CRYSTAL STRUCTURES AND COMPUTATIONAL METHODS

A. Symmetry and shift conductivity tensor

Single hexagonal BN sheet is a noncentrosymmetric crystal with space group $P\bar{6}m2$ and point group D_{3h}, a symmetry analysis would show that the single BN sheet has three nonzero shift conductivity tensor elements σ^{xxy}, σ^{yxx}, and σ^{yyy}, where the first Cartesian index is the direction of the current and the second and third indices are the polarization directions of the external field. Furthermore, $\sigma^{xxy} = \sigma^{yxx} = -\sigma^{yyy}$ [11,22], i.e., there is only one independent nonzero element. As an example, let us consider the difference between in-plane shift conductivity tensor elements σ^{xxx} and σ^{yyy} in the single BN sheet [see Fig. 1(c)]. Figure 1(c) indicates that the atomic structures on the left and right regions to the mirror plane (denoted by the dashed line) (the y axis) are symmetric. Therefore, the shift current along the direction normal to the mirror plane (the x axis) would be zero if the second-order combination of external fields is even under the mirror symmetry, i.e., $\sigma^{xxx} = 0$. On the other hand, such mirror symmetry does not exist in the direction along the mirror plane (the y axis), and thus the conductivity element σ^{yyy} would not be zero.

When a hexagonal BN sheet is wrapped up to form a zigzag BN-NT with chiral index $(n, 0)$, the y axis would become the tube axis [the c axis, see Fig. 1(a)] and the point group of the resultant BN-NT $(n,0)$ is C_{2nc}. Thus, the conductivity tensor element σ^{ccc} is nonzero. On the other hand, there is no azimuthal shift current in the zigzag BN-NTs because it corresponds to the direction of the x axis in the single BN sheet (see Fig. 1).

B. Density functional theory calculations

Ab initio calculations, based the density functional theory (DFT) with the local density approximation (LDA), are performed to determine the ground-state properties of the considered zigzag BN-NTs and also the single BN sheet. A supercell geometry is adopted to simulate a BN-NT in which the nanotubes are arranged in a square array with a minimum distance of 12 Å between the neighboring nanotubes. A slab supercell method is used to model the single BN sheet, and the intersheet distance used is over 16 Å. In the structural optimization calculations, the accurate projector-augmented wave (PAW) method plus the conjugate gradient approach, as implemented in the VASP package [23,24], is used to determine the atomic positions and lattice constants of BN-NTs. A large plane-wave cutoff energy of 450 eV is adopted. Theoretical equilibrium structures are obtained when the forces acting on all the atoms and the uniaxial stress were less than 0.005 eV/Å and 2.0 kBar, respectively.

The ground electronic structure calculations are performed by using the plane-wave pseudopotential method as implemented in the QUANTUM ESPRESSO package [25]. The optimized norm-conserving Vanderbilt pseudopotential [26] is exploited here. The $1 \times 1 \times 32$ and $18 \times 18 \times 1$ Monkhorst-Pack k grids [27] are used to evaluate the Brillouin zone (BZ) integrals for the BN-NTs and the single BN sheet, respectively. The energy cutoff for the plane-wave basis set is 50 Ry. The resultant electronic structures are used in the subsequent GW-BSE calculations, as described below.

C. Quasiparticle band structure calculations

The present GW-BSE calculations are performed via the BERKELEYGW package [28–30]. The quasiparticle energy bands are calculated by solving the Dyson equation

$$\left[-\frac{1}{2}\nabla^2 + V_{\text{ion}} + V_{\text{H}} + \Sigma\left(E_{n\mathbf{k}}^{\text{QP}}\right)\right]\psi_{n\mathbf{k}}^{\text{QP}} = E_{n\mathbf{k}}^{\text{QP}}\psi_{n\mathbf{k}}^{\text{QP}}, \quad (1)$$

where Σ, $E_{n\mathbf{k}}^{\text{QP}}$, and $\psi_{n\mathbf{k}}^{\text{QP}}$ are the self-energy operator, the energy, and the wave function of the quasiparticles within the G_0W_0 approximation, respectively [30].

In the present one-shot G_0W_0 calculations [31], a nonuniform neck subsampling (NNS) k grid of $1 \times 1 \times 8$ ($18 \times 18 \times 1$) with a subsampling of 10 points in the mini-Brillouin zone, 600 (2000) bands, and a dielectric cutoff energy of 50 (50) Ry for the BN-NTs (the single BN sheet) are used. Truncation of the Coulomb interactions between the BN-NT (the BN sheet) and its periodic images is implemented [32]. The dynamic dielectric matrix is computed within the independent particle approximation (IPA) and Hybertsen-Louie generalized plasmon pole model [28].

D. Exciton excitation calculations

The exciton wave function can be expressed as the linear combination of the quasiparticle electron-hole pairs,

$$\Psi_s(\mathbf{r}_e, \mathbf{r}_h) = \sum_{\mathbf{k},m,n} A_{mn\mathbf{k}}^s \psi_{n\mathbf{k}}^{\text{QP}}(\mathbf{r}_e)\psi_{m\mathbf{k}}^{\text{QP}*}(\mathbf{r}_h), \quad (2)$$

where band index m (n) sums over the valence (conduction) bands only. Exciton envelope function of the sth exciton state $A_{mn\mathbf{k}}^s$ can be obtained by solving the BSE,

$$\sum_{m'n'\mathbf{k}'} \left[\left(E_{n\mathbf{k}}^{\text{QP}} - E_{m\mathbf{k}}^{\text{QP}}\right)\delta_{nn'}\delta_{mm'}\delta_{\mathbf{k}\mathbf{k}'} + \langle mn\mathbf{k}|K^{eh}|m'n'\mathbf{k}'\rangle\right]A_{m'n'\mathbf{k}}^s = \Omega^s A_{mn\mathbf{k}}^s, \quad (3)$$

where Ω^s and $E_{m\mathbf{k}}^{\text{QP}}$ ($E_{n\mathbf{k}}^{\text{QP}}$) are the sth exciton excitation energy and the valence (conduction) band quasiparticle excitation energies with the band index m (n) and the crystal momentum $\mathbf{k}$, respectively. K^{eh} is the electron-hole interaction kernel, which includes an exchange repulsive bare Coulomb term and a direct electron-hole attractive screened Coulomb term [29,30]. The imaginary part of the dielectric function including the excitonic effect can be expressed as

$$\varepsilon''_{\text{BSE}} = \frac{g_s\pi e^2}{\epsilon_0 N_k V_c}\sum_s \left|\sum_{mn\mathbf{k}} A_{nm\mathbf{k}}^s \mathbf{x}_{mn\mathbf{k}} \cdot \mathbf{e}\right|^2 \delta(\omega - \Omega^s) = \frac{g_s\pi e^2}{\epsilon_0 N_k V_c}\sum_s |\mathbf{X}_s \cdot \mathbf{e}|^2 \delta(\omega - \Omega^s), \quad (4)$$

where $\mathbf{e}$ denotes the polarization direction, and g_s accounts for the spin degeneracy. N_k is the number of k points and V_c is the unit-cell volume. The dipole matrix element is $\mathbf{x}_{mn\mathbf{k}} = \langle u_{m\mathbf{k}}|i\nabla_{\mathbf{k}}|u_{n\mathbf{k}}\rangle$, where $|u_{n\mathbf{k}}\rangle$ ($\langle u_{m\mathbf{k}}|$) is the cell-periodic part of the wave function $|\psi_{n\mathbf{k}}^{\text{QP}}\rangle$ ($\langle\psi_{m\mathbf{k}}^{\text{QP}}|$).

The exciton dipole matrix element $\mathbf{X}_s$ is defined as

$$\mathbf{X}_s \equiv \sum_{mn\mathbf{k}} A_{nm\mathbf{k}}^s \mathbf{x}_{mn\mathbf{k}}. \quad (5)$$

When neglecting the excitonic effect, optical excitations are given by direct transitions between the energy levels of the quasiparticles in the electron-hole pairs. Within the IPA approximation, the imaginary part of the dielectric function reduces to [29]

$$\varepsilon''_{\text{IPA}} = \frac{g_s\pi e^2}{\epsilon_0 N_k V_c}\sum_{mn\mathbf{k}} |\mathbf{x}_{mn\mathbf{k}} \cdot \mathbf{e}|^2 \delta\left(\omega - \left(E_{n\mathbf{k}}^{\text{QP}} - E_{m\mathbf{k}}^{\text{QP}}\right)\right). \quad (6)$$

Equation (4) has the same structure as Eq. (6) except that the dipole matrix element is replaced by the exciton dipole matrix element. Our BSE calculations for the BN-NTs (the single BN sheet) are computed on a dense k grid of $1 \times 1 \times 64$ ($72 \times 72 \times 1$) with the dielectric cutoff of 10 (10) Ry.

E. Exciton shift current calculations

The shift current density along the a axis is given by [4]

$$J^a_{sh}(\omega) = 2\sum_{bc}\sigma^{abc}(0;\omega,-\omega)E^b(\omega)E^c(-\omega), \tag{7}$$

where σ^{abc} is the third-rank conductivity tensor, b and c denote the polarization directions of the electric fields of the incident light. In the IPA, σ^{abc} can be expressed as [4,33]

$$\begin{aligned}\sigma^{abc}(0;\omega,-\omega) = -\frac{i\pi e^3}{4N_k V_c}\sum_{n,m,\mathbf{k}} f_{nm\mathbf{k}}\big(x^b_{mn\mathbf{k}}\big[x^c_{nm\mathbf{k}}\big]_{;k_a}\\ + x^c_{mn\mathbf{k}}\big[x^b_{nm\mathbf{k}}\big]_{;k_a}\big)[\delta(\omega_{mn\mathbf{k}}-\omega)\\ + \delta(\omega_{nm\mathbf{k}}-\omega)],\end{aligned} \tag{8}$$

where $x^a_{nm\mathbf{k}}$ and $[x^a_{nm\mathbf{k}}]_{;\mathbf{k}}$ are the dipole matrix element and its generalized momentum derivative, respectively. The generalized momentum derivative of quantity $O_{mn\mathbf{k}}$ is given by

$$\big[O^b_{nm\mathbf{k}}\big]_{;k_a} = \partial_{k_a}O^b_{nm\mathbf{k}} - i\big[\xi^a_{nn\mathbf{k}} - \xi^a_{mm\mathbf{k}}\big]O^b_{nm\mathbf{k}}, \tag{9}$$

where $\xi^a_{nm\mathbf{k}}$ is the a component of the Berry connection [4]. $f_{nm\mathbf{k}} = f_{n\mathbf{k}} - f_{m\mathbf{k}}$ and $\hbar\omega_{nm\mathbf{k}} = E^{\mathrm{QP}}_{n\mathbf{k}} - E^{\mathrm{QP}}_{m\mathbf{k}}$ where $f_{n\mathbf{k}}$ denotes the occupation factor of the nth band at the $\mathbf{k}$ point. Note that here band indices m and n should sum over all the states.

As mentioned before, to include the excitonic effect, we use the efficient perturbative density-matrix approach to calculate σ^{abc} [see Eq. (B1a) in Ref. [21]]. In this case, σ^{abc} can be written as

$$\begin{aligned}\sigma^{abc}(0,\omega,-\omega) = -\frac{g_s e^3}{2N_{\mathbf{k}}V_c}\sum_{ss'}\Bigg[\frac{X^b_s\Pi^a_{ss'}X^{c*}_{s'}}{(\hbar\omega-\Omega^s+i\eta)(\hbar\omega-\Omega^{s'}-i\eta)} + \frac{V^{a*}_s X^b_{ss'}X^c_{s'}}{-\Omega^s(\hbar\omega-\Omega^{s'}+i\eta)} + \frac{V^a_s X^{b*}_{ss'}X^{c*}_{s'}}{-\Omega^s(-\hbar\omega-\Omega^{s'}-i\eta)}\Bigg]\\ + (b\leftrightarrow c,\omega\leftrightarrow-\omega),\end{aligned} \tag{10}$$

where we define $V^a_s \equiv \sum_{cv\mathbf{k}} A^{s*}_{cv\mathbf{k}}v^a_{cv\mathbf{k}}$ with velocity matrix elements $v^a_{cv\mathbf{k}}$, and interexciton coupling matrix elements $X_{ss'}$ and $\Pi_{ss'}$ are defined as

$$\Pi^a_{ss'} \equiv \sum_{cvc'\mathbf{k}} A^s_{cv\mathbf{k}}v^a_{c'c\mathbf{k}}A^{s'*}_{c'v\mathbf{k}} - \sum_{cvv'\mathbf{k}} A^s_{cv'\mathbf{k}}v^a_{v'v\mathbf{k}}A^{s'*}_{cv\mathbf{k}},$$

and $X^b_{ss'} = Y^b_{ss'} + Q^b_{ss'}$. We note that c and v denote that the summation runs over the conduction and valence band, respectively. Here, $\mathbf{X}_{ss'}$ is an ill-defined operator. However, it can be separated into the well-defined $\mathbf{Y}_{ss'}$ (interband part) and $\mathbf{Q}_{ss'}$ (intraband part) operators, where

$$Q^b_{ss'} = i\sum_{c'v'\mathbf{k}'} A^{s*}_{c'v'\mathbf{k}'}\big(A^{s'}_{c'v'\mathbf{k}'}\big)_{;k'_b}$$

and

$$Y^b_{ss'} = \sum_{\substack{c'\neq c_1\\ v'\neq v_1}}\sum_{c_1v_1\mathbf{k}} A^{s*}_{c'v'\mathbf{k}'}\big[A^{s'}_{c_1v'\mathbf{k}'}x^b_{c'c_1} - A^{s'}_{c'v_1\mathbf{k}'}x^b_{v_1v'}\big].$$

We develop a postprocessing program to implement Eq. (10), which is then used to calculate the excitonic shift current conductivity using the outputs from the BERKELEYGW package.

It is not straightforward to evaluate the intraband portion of the position operator $\mathbf{Q}_{ss'}$ since it involves the numerical derivative of the exciton envelope function $A^s_{nm\mathbf{k}}$ with respect to $\mathbf{k}$. Furthermore, $A^s_{nm\mathbf{k}}$ has an arbitrary k-dependent gauge. To solve the problem, we use the locally smooth gauge adopted in Ref. [8] to calculate the intraband position operator. The idea of the locally smooth gauge is to rotate the wave functions at neighboring k points in such a way that the overlap of connected wave functions is Hermitian [8,34,35].

In this work, the δ function is approximated by a Gaussian function with a 0.1-eV broadening. To estimate the effective three-dimensional (3D) conductivity, we use the effective unit-cell volume rather than the supercell volume for the BN-NTs and single BN sheet. The effective unit-cell volume for a BN-NT is given by $V_c = \pi[(D/2+d/2)^2-(D/2-d/2)^2]T = \pi DdT$, where D is the tube diameter, T is the length of translational vector, and d is the effective thickness of the nanotube walls, which is set to the interlayer distance (3.28 Å) of h-BN [19]. For the single BN sheet, the effective unit-cell volume is $V_c = A_c d$ where A_c and d are the area of the unit cell and effective thickness of the sheet, respectively.

III. RESULTS AND DISCUSSION

A. Electronic and optical properties of the single BN sheet

Both the *GW* and LDA quasiparticle band structures of the single BN sheet are displayed in Fig. 2. Our *GW* quasiparticle band structure agrees well with the previous calculations [36–42]. The single BN sheet shares the similar structure with graphene, the honeycomb lattice. However, unlike graphene which is a semimetal with π and π^* bands degenerate at the K point, here the π and π^* bands are well separated due to the ionicity difference between B and N [32]. Hence, the single BN sheet has a large band gap (Fig. 2). Table I shows that the single BN sheet is an insulator with a $K^v \rightarrow K^c$ direct band gap of 4.65 eV from the LDA calculation. However, the single BN sheet becomes an insulator with a larger $K^v \rightarrow \Gamma^c$ indirect band gap of 7.66 eV from the *GW* calculation. The large *GW* quasiparticle correction to the LDA band gap can be attributed to the weak dielectric screening, a consequence of 2D nature and the wide band gap of the BN sheet. The *GW* quasiparticle correction of the $K^v \rightarrow K^c$ gap (3.26 eV) is slightly (0.37 eV) larger than that of $K^v \rightarrow \Gamma^c$ (2.89 eV). This makes the single BN sheet transform from the direct band gap ($K^v \rightarrow K^c$) in the LDA to the indirect band gap ($K^v \rightarrow \Gamma^c$) at the *GW* level. The π^* band, arising from $2p_z$ orbitals, has the out-of-plane charge density and hence the weaker dielectric screening. The weaker dielectric screening of the π^* band explains why the quasiparticle correction of $K^v \rightarrow K^c$ gap is smaller than that of

TABLE I. Transition energies from the valence band maximum (v) to conduction band minimum (c) (ΔE), band gaps (E_g), bandwidths, the onset of the continuum optical absorption ($E_{\rm abs}$), exciton excitation energy (i.e., optical band gap) (Ω), and exciton binding energy (E_b) of a single BN sheet. The available experimental data (Expt.) are also listed for comparison.

	ΔE (E_g) (eV)		$E_{\rm abs}$ (eV)	Bandwidth (eV)			Ω (eV)	E_b (eV)
	$K^v \rightarrow K^c$	$K^v \rightarrow \Gamma^c$		π band	σ_1 band	σ_2 band	Exciton A (B)	
LDA	4.65 (4.65)	4.77	4.52	5.45	5.80	7.65	...	...
GW	7.91	7.66 (7.66)	7.72	5.93	6.41	8.20	...	...
GW-BSE	...	...	...	...	...	...	5.91 (6.76)	1.81 (0.96)
Expt.	...	...	...	5.8[a]	6.5[a]	8.2[a]	6.05[b], 6.03[c], 6.1[d]	...

[a] Reference [44].
[b] Reference [45].
[c] Reference [46].
[d] Reference [47].

$K^v \rightarrow \Gamma^c$ gap [43]. Consequently, the *GW* quasiparticle correction not only modifies the band gap, but also changes the dispersion of the bands. This indicates the significance of *GW* quasiparticle calculations, and thus the complex screening effect cannot be fully taken into account through a simple scissor correction. We notice that our *GW* bandwidths are in nearly perfect agreement with the experimental values (Table I).

Figure 3(a) shows the calculated imaginary (absorptive) part (ε'') of the dielectric function of the single BN sheet. We notice that the ε'' spectrum looks very similar to that of the previous LDA calculation [19], *albeit* with the onset of the absorption and peak positions at much higher photon energies due to the *GW* quasiparticle corrections. For optical excitations below 10 eV with the in-plane polarization of the electric field, only transitions between the π and π^* bands are dipole allowed. The oscillator strength of the dielectric function is mainly contributed by the π and π^* bands. The onset energy of the absorption spectrum at the *GW*-IPA level corresponds to the direct transition at the K point. On the other hand, the optical transition near the M point contributes to the largest peak at ~9.0 eV. In other words, the oscillator strength of the dielectric function stems primarily from the optical transitions between two flat π and π^* bands along the high symmetry K-M line.

Remarkably, when the excitonic effect is included at the *GW*-BSE level, two prominent absorption peaks [labeled A

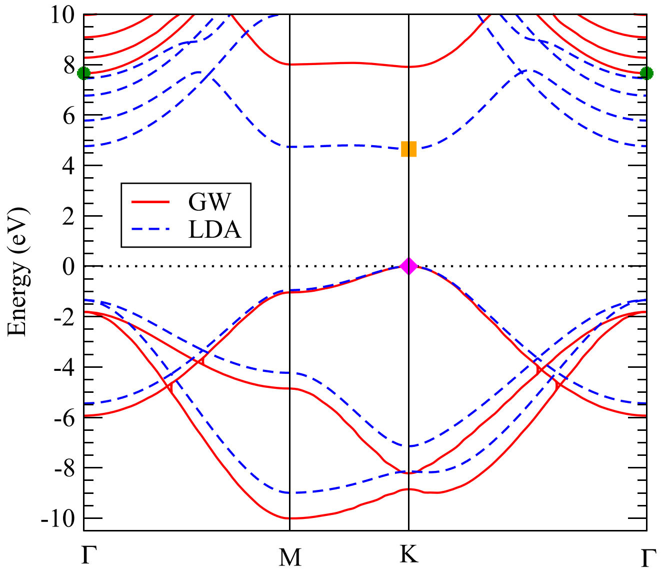

FIG. 2. Quasiparticle band structure of the single BN sheet from our *GW* (solid red lines) and LDA (blue dashed lines) calculations. Valence band maximum is set at 0 eV, which is at the K point indicated by the pink diamond. The conduction band minima of the *GW* and LDA band structures are denoted by the green dot at the Γ and orange square at the K point, respectively.

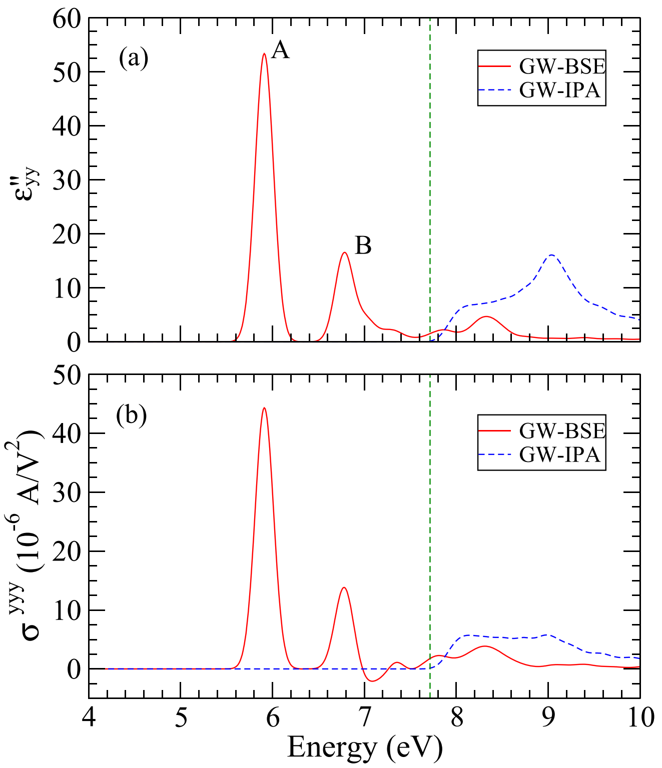

FIG. 3. (a) Imaginary part of the dielectric function and (b) shift current conductivity of the single BN sheet from both *GW*-BSE (solid red line) and *GW*-IPA (dashed blue line) calculations. The first two bright exciton peaks are labeled by A and B. The green vertical line indicates the onset of the continuum optical absorption (see Table I).

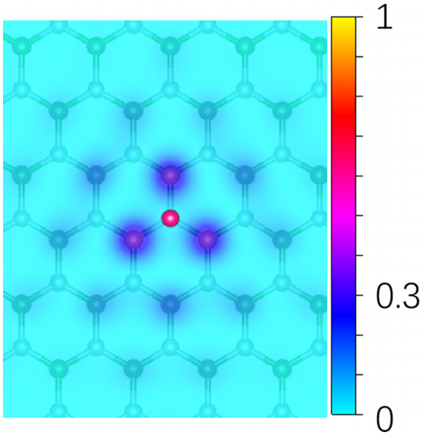

FIG. 4. The electron probability distribution $|\psi(\mathbf{r}_e, \mathbf{r}_h)|^2$ [see Eq. (2)] of the doubly degenerate *A* exciton in the single BN sheet with the hole position ($\mathbf{r}_h$) fixed at the N atom (the pink sphere).

and *B* in Fig. 3(a)] occur in the quasiparticle band gap and they are due to the excitation of the first two bright excitons. Unlike bulk semiconductors such as CdS in which the exciton peak usually appears a shoulder on the absorption edge [9], the *A* and *B* exciton peaks in the single BN sheet are completely detached from the quasiparticle absorption edge due to their large binding energies of 1.81 and 0.96 eV (Table I), respectively. Note that the exciton binding energy of CdS is only 30 meV. We also notice that the calculated large excitation energy of the *A* exciton agrees well with the measured optical band gap (see Table I).

The large exciton binding energies are the consequence of the weak screening in 2D wide-band-gap materials such as the single BN sheet, as mentioned in the previous paragraph. Figure 4 shows the exciton *A* wave function ($|\psi(\mathbf{r}_e, \mathbf{r}_h)|^2$). Clearly, the exciton is strongly localized, and the electron probability distribution beyond the nearest neighbor is lower than 30%. Consequently, the exciton envelope function of the *A* exciton is widespread in the BZ [36], resulting in the mixing between the interband electron-hole excitations along the high-symmetry *K*-*M* line. The mixing strongly redistributes the oscillator strength of the spectrum [see Eq. (4)]. The in-gap exciton states *A* and *B* carry almost all the oscillator strength, and the absorption spectrum almost diminishes above the quasiparticle band gap. The magnitude of the *A* exciton peak is more than three times larger than the largest quasiparticle absorption peak at ~9.0 eV at the *GW*-IPA level.

Figure 3(b) displays the calculated shift current conductivity of the BN sheet. Clearly, the shift current conductivity spectra are rather similar to the corresponding absorption spectra. In particular, when the excitonic effect is included, two distinguished peaks occur within the quasiparticle band gap (red line). Comparing the shift current conductivity to the imaginary part of the dielectric function indicates that the two peaks are due to the *A* and *B* excitons. The height of the maximal peak at 5.91 eV is nearly eight times larger than that of the shoulder at 8.15 eV from the *GW*-IPA calculation, i.e., the effect of the exciton not only creates two in-gap peaks but also greatly enhances the shift current. The significant increase in the shift current is primarily due to the in-gap *A* exciton, and is mainly caused by the significant enhancement of the optical dipole matrix element [see Eqs. (4) and (10)] due to strong overlap of wave functions of the electron and hole within the electron-hole pair.

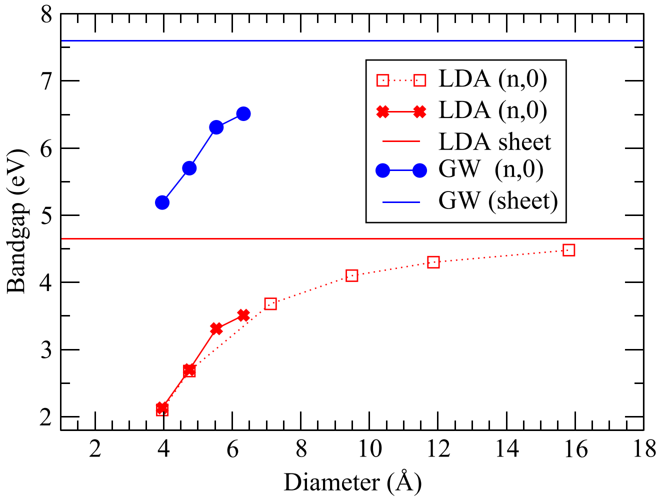

FIG. 5. Quasiparticle band gaps of the zigzag BN-NTs vs the tube diameter from both LDA and *GW* calculations. Band gaps from the previous LDA calculation [19] are denoted by red open squares. The horizontal red and blue lines indicate the quasiparticle band gaps of the single BN sheet from the LDA and *GW* calculations, respectively.

B. Electronic properties of BN nanotubes

Our LDA and *GW* calculations indicate that the zigzag BN-NTs considered here are direct band-gap insulators with $\Gamma^v \rightarrow \Gamma^c$ transition, being consistent with previous LDA calculations (see, e.g., Ref. [19]). The calculated band gaps of the zigzag BN-NTs are listed in Table II and also displayed in Fig. 5. Figure 5 shows that for small-diameter BN-NTs, both *GW* and LDA band gaps get reduced dramatically as the diameter decreases. Interestingly, the *GW* correction to the LDA band gap (ΔE_g) is almost independent of the diameter, being about 3.0 eV (Table II and Fig. 5). The lowering of the band gap relative to the BN sheet already occurs at the LDA level [19], and was attributed to the curvature-induced orbital rehybridization. The π^* and σ^* orbitals are orthogonal to each other in the flat BN sheet. However, such orthogonality does not hold in the BN-NTs where the local curvature exists. Consequently, the π^* and σ^* orbitals can hybridize and form ringlike charge distribution, as shown in Fig. 6. The ring-like charge distribution can effectively reduce the ionicity and hence lowers the energies of π^* bands [48–50], thereby reducing the quasiparticle band gaps of the BN-NTs. As the diameter increases, the effect of curvature-induced orbital rehybridization decreases and the band gap converges to that of a single BN sheet.

C. Absorption spectra of BN nanotubes

We show the calculated absorptive part (ε'') of the dielectric function of the considered BN-NTs and also single BN sheet in Fig. 7(a). In the BN-NTs, optical transitions between

TABLE II. Diameter (D), band gap (E_g), the onset of the continuum optical absorption (E_{abs}), exciton excitation energy (Ω), exciton binding energy (E_b), and the difference between the LDA and GW band gaps ($\Delta E_g^{GW-\text{LDA}}$) of the zigzag BN-NTs and also single BN sheet (Table I). For comparison, the measured optical band gaps (Ω) of large-diameter BN-NTs are also listed.

					Exciton A		
	D (Å)	E_g^{LDA} (eV)	E_g^{GW} (eV)	$\Delta E_g^{GW-\text{LDA}}$ (eV)	E_{abs} (eV)	E_b (eV)	Ω (eV)
BN-NT							
(5,0)	4.11	2.13	5.19	3.06	7.06	2.23	4.83
(6,0)	4.87	2.70	5.70	3.00	7.37	2.32	5.05
(7,0)	5.65	3.31	6.31	3.00	7.61	2.27	5.34
(8,0)	6.43	3.51	6.51	3.00	7.71	2.28	5.43
Expt.[a]	<10	...	...	...	...	...	5.51
Expt.[b]	15-30	...	...	...	...	...	5.8 ± 0.2
Expt.[c]	50 ± 10	...	...	...	...	...	5.82 ± 0.01
Expt.[c]	600 ± 100	...	...	...	...	...	5.90 ± 0.01
Sheet	∞	4.65	7.66	3.01	7.72	1.81	5.91

[a] Reference [15].
[b] Reference [51].
[c] Reference [16].

π and π^* bands dominate the absorption spectra. First, compared with the single BN sheet, the energies of the π^* bands of the BN-NTs are lowered owing to the curvature-induced orbital rehybridization, as discussed above. Consequently, the energies of the ε'' continuum onset at the GW-IPA level decrease with decreasing diameter, as shown in Fig. 7(a) and Table II. Second, contrary to the moderate diameter (D >10 Å) BN-NTs where the ε'' spectrum consists of a single distinct peak [19], the absorption spectra of the small-diameter BN-NTs considered here feature multiple peaks at the GW-IPA level. For example, the ε'' spectrum of BN-NT (5,0) possesses three distinct peaks at 7.4, 7.9, and 8.7 eV, respectively.

BN-NTs are 1D wide-band-gap insulators. Consequently, due to much reduced dielectric screening in these 1D wide-band-gap materials, large exciton binding energies arise. For small-diameter BN-NT (5,0), in particular, the exciton binding energy E_b of peak A is 2.23 eV, which is larger than that

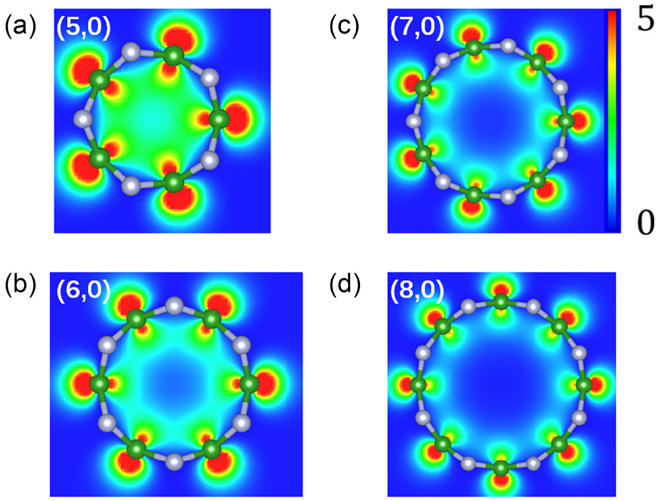

FIG. 6. Charge density distribution (in units of 10^{-3} Å^{-3}) of the states in the vicinity of the conduction band minimum of the zigzag [(5,0), (6,0), (7,0), (8,0)] BN-NTs. B and N atoms are indicated by green and gray spheres, respectively.

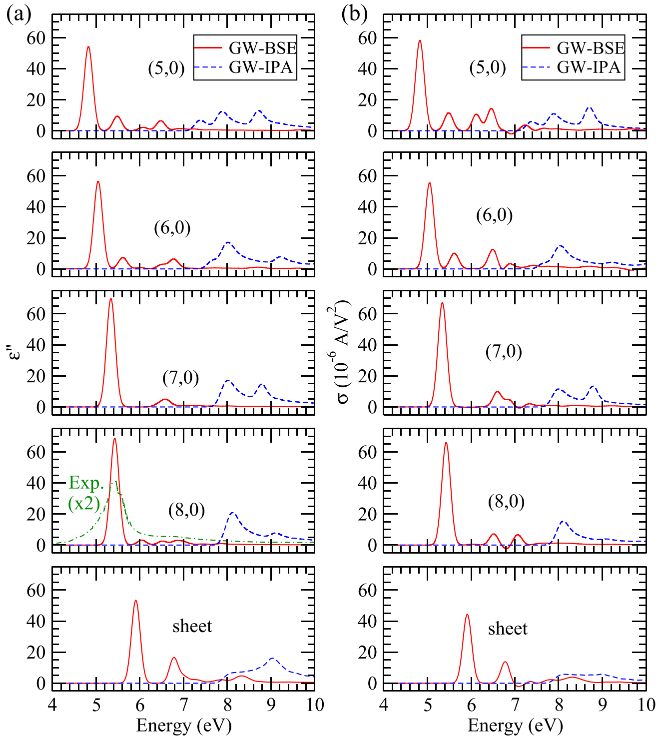

FIG. 7. (a) The imaginary (absorptive) part of the dielectric function and (b) shift current conductivity of the single-walled zigzag [(5,0), (6,0), (7,0), (8,0)] BN-NTs and the single BN sheet from both the GW-BSE (solid red lines) and GW-IPA (dashed blue lines) calculations. The prominent peak labeled A is due to the first bright exciton (exciton A). Both the polarization direction of light electric field [(a) and (b)] and shift current (b) are parallel to the tube axis (y axis) in the BN-NTs (BN sheet). For comparison, the experimental dielectric function of the multiwalled BN-NT [52] is also displayed in (a).

(1.81 eV) of the 2D single BN sheet (Table I) and also that (0.63 eV) of the typical 2D transition metal dichalcogenide semiconductor $\mathrm{MoS_2}$ [53]. It is also much larger than that of 3D bulk h-BN (0.72 eV) [54] and 2H-$\mathrm{MoS_2}$ (0.05) [55]. Note that the exciton binding energy of typical bulk semiconductor CdS is as small as 0.03 eV [9]. The large E_b results in the emergence of the huge in-gap absorption peak which is completely detached from the onset of the continuum absorption ε'' spectrum of the BN-NT. Most of the oscillator strength of ε'' spectra is carried by the A exciton state of the BN-NTs.

Table II shows the excitation energies (Ω) of exciton A in BN-NTs. Our calculated Ω converges to that of the single BN sheet and agrees well with the experimental values [16,51]. We also compare our calculated ε'' with the experimental one derived from electron energy-loss spectra. Experimental ε'' of medium-diameter multiwalled BN-NTs with small momentum transfer $q = 0.1$ Å^{-1} is plotted in Fig. 7(a) (green dash-dotted line) [52]. The complex main peak at 5.5 eV in the experimental ε'' spectrum may consist of exciton A peaks from different walls of the multiwalled BN-NT. The substantial broadening of the complex primary peak could be due to the consequence of the finite exciton lifetime. The shoulder from around 6.0 to 8.0 eV may be contributed by minor peaks other than exciton A peak.

In the low-dimensional BN systems, exciton A is strongly localized, as shown in Fig. 4. The localized nature of exciton A suppresses the curvature effect on the exciton binding energy as the tube diameter increases, and leads to the fast convergence of the exciton binding energy (see Table II) [13]. The redshift of the A peak can be attributed to the curvature-induced orbital rehybridization that lowers the energies of π^* bands and reduces the onset of the continuum ε'' at the GW-IPA level.

D. Exciton shift current of BN nanotubes

In Fig. 7(b), calculated shift current conductivity spectra of the BN-NTs are plotted. Figure 7 shows that the shift current spectra are very similar to the corresponding ε'' spectra. This correlation is facilitated by the dipole matrix elements present in both the expressions for ε'' [Eq. (4)] and the expression for the shift current [Eq. (8)]. In particular, as for the ε'' spectrum, the strong excitonic effect results in the occurrence of the large in-gap shift current peak from the GW-BSE calculation [Fig. 7(b)]. The prominent shift current peak in the BN-NTs and single BN sheet is due to the excitation of the A exciton. Furthermore, the excitonic effect substantially increases the largest shift current peak of all the BN-NTs by nearly a factor of 3. This large enhancement of the shift current by the A exciton is mainly due to the large enhancement of the dipole matrix element caused by the strong overlap of the wave functions of the electron and hole in the A exciton state.

Interestingly, unlike the excitonic peak A, the excitonic peak B in both the absorption and shift current spectra does not change monotonically as the diameter of the BN-NTs decreases (see Fig. 7). We attribute this to the fact that the excitons of the secondary (B) peak in a single BN sheet and in the BN-NTs could have quite different characters. In the single BN sheet, the B peak excitons are 2p-like states, as also reported in [36]. Here we find that the lowest-energy p-like states in the BN-NTs are dark and the B peak excitons are quite diverse in their characters. In the (5,0), (6,0), and (8,0) BN-NTs, the B exciton with excitation energies of 5.48, 6.8, and 6.05 eV, respectively, are either s like or have mixed characters. Nevertheless, in the (7,0) BN-NT, the B exciton does have a p-like wave function.

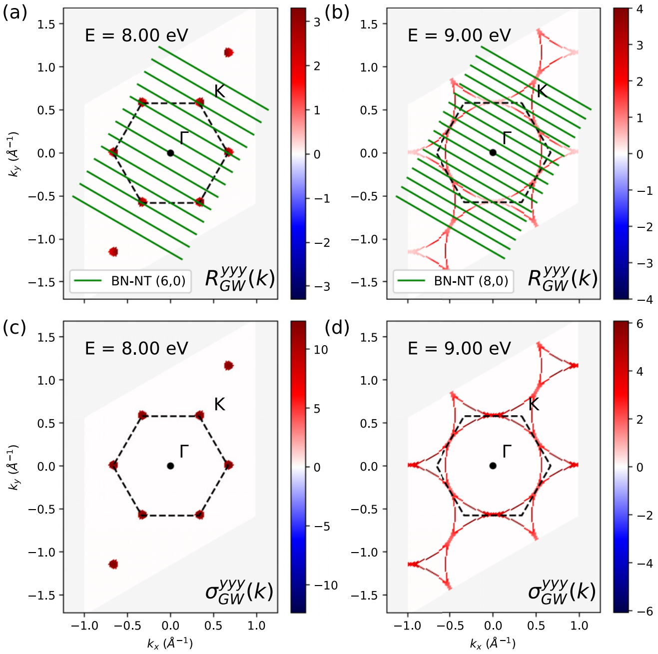

FIG. 8. The **k**-resolved shift vector (R) (a), (b) and shift current conductivity (σ) (c), (d) of the single BN sheet from the GW-IPA calculation. The units of the color bars for R and σ are Å and μA/V^2, respectively. The green lines in (a) and (b) indicate the 1D BZ of the (6,0) and (8,0) BN-NTs, respectively.

The optical responses of BN-NTs in the low-energy region are dominated by π-π^* transitions. As mentioned before, the curvature-induced orbital rehybridization lowers the energy of the π^* bands of BN-NTs. As a result, the onset of the shift current spectra at the GW-IPA level decreases with decreasing diameter, as shown in Fig. 7(b). Similar to ε'' spectra, shift current spectra of small-diameter BN-NTs feature multiple peaks at the GW-IPA level.

Figure 7(b) shows that the shift current spectra of the $(n, 0)$ BN-NTs from both *ab initio* GW-IPA and GW-BSE calculations do not change sign as the tube diameter (or n) increases, i.e., the direction of the calculated shift current does not follow the simple rule of $\mathrm{sgn}(J_{\mathrm{shift}}) = \mathrm{mod}(n, 3)$ predicted by the previous tight-binding model calculations [17,18]. To better understand this important finding, we compute the **k**-resolved shift conductivity and shift vector, which is given by $R^{yyy}_{GW\text{-IPA}}(\mathbf{k}) = \mathrm{Im}[\mathbf{x}^y_{mn}[\mathbf{x}^y_{nm}]_{;k_y}]/|\mathbf{x}^y_{mn}|^2$ where m and n refer to the lowest conduction band and highest valence band, respectively [56], of the single BN sheet, as displayed in Fig. 8 for two incident photon energies of 8.0 (optical absorption edge) and 9.0 eV (the peak position) at the GW-IPA level. Figure 8 indicates that the **k**-resolved shift current and shift vector of the single BN sheet are positive in the whole BZ for both selected photon energies. At the absorption edge (8.0 eV), the shift current and shift vector are localized on the K and K' points. As the energy increases to the peak position (9.0 eV), the weights of the shift current and shift vector extend toward the M point and eventually toward the K-Γ symmetry line. The 1D BZ of one BN-NT consists of a few discrete lines on the 2D BZ of the BN sheet [10], as displayed for the (6,0) and (8,0) BN-NTs in Fig. 8. Consequently, the direction of the shift current of the zigzag $(n, 0)$ BN-NTs would remain unchanged when the tube diameter [or the chirality $(n, 0)$] varies, contrary to the prediction of the model calculations [17,18].

We notice that previous model calculations also predicted that the direction of the electric polarization of the zigzag BN-NTs would follow the same rule of $\mathrm{sgn}(J_{\mathrm{shift}}) = \mathrm{mod}(n, 3)$ as the shift current [17,57]. This is not surprising since the electric polarization and shift current are closely connected [58]. However, a subsequent *ab initio* calculation showed that the electric polarization of the zigzag BN-NTs grows monotonically as the tube diameter increases [59], i.e., the direction of the electric polarization does not depend on the chiral index (n). Therefore, both the previous [59] and present *ab initio* calculations demonstrate the importance of the full *ab initio* calculations for the electric polarization and shift current in the BN-NTs.

Furthermore, a close examination of the simple tight-binding model Hamiltonian suggests that the erroneous prediction of the tight-binding model calculations [17,18] would stem from the fact that only π bands in the single BN sheet and hence the transitions between the lowest two azimuthal subbands in zigzag BN-NTs were included, whereas the predominant exciton peak in BN-NTs is composed of a coherent supposition of transitions from several different subband pairs [14]. Consequently, the rehybridization effect, induced by the curvature of small-diameter BN-NTs, is missing in the simple tight-binding method [17,18]. Indeed, previous DFT calculations showed that the rehybridization effect plays a crucial role in the strong band-gap renormalization for small-diameter zigzag BN-NTs [19].

Let us now compare the magnitude of the excitonic photocurrents in the considered BN systems with the observed shift currents in well-known materials. First, the observed photocurrent in ferroelectric $\mathrm{BaTiO_3}$ above the absorption edge under light intensity $I = 0.5\ \mathrm{mW/cm^2}$ and sample width $w = 0.15$ cm is around 5×10^{-13} A [60]. We find that under the same conditions, the A exciton shift current of a single BN sheet would reach 5.0×10^{-12} A, and that from a thin film consisting of, e.g., the (5,0) BN-NT array with an intertubular distance (d) of 3.28 would be as large as $\sim$10 mA. Second, the effective conductivity of the A exciton shift current in the considered BN systems (Fig. 7) is about two orders of magnitude larger than the excitonic shift conductivity ($\sim$0.2 $\mu\mathrm{A/V^2}$) observed in semiconductor CdS [9], and also more than five times larger than the largest observed shift conductivity ($\sim$10.0 $\mu\mathrm{A/V^2}$) in ferroelectric SbSI [61].

Finally, it appears that for the steady state, the excitation and recombination processes might cancel out the total exciton shift current [62]. However, a total cancellation could be avoided by the subtle role of dissipation, as discussed recently in Refs. [63,64], which is applicable for both excitonic and quasiparticle shift currents. Microscopic irreversible processes such as defect- and exciton-phonon scattering, which results in the finite quasiparticle lifetime, would prevent the backward shift current to completely cancel out the generated current.

IV. CONCLUSIONS

Using the newly developed computationally efficient algorithms, we have performed the state-of-the-art *ab initio* *GW*-BSE calculations to investigate the exciton shift current as well as the electronic and optical properties of the zigzag [(5,0), (6,0), (7,0), (8,0)] BN-NTs and also the single BN sheet. First of all, we find a large in-gap peak in both the shift current and optical absorption spectra in all the studied BN systems due to the A exciton. This excitonic peak is nearly three times higher than that in the continuum due to the excitation of the free electron-hole pairs (Fig. 7), and may be attributed to the significant enhancement of the optical dipole matrix element by the A exciton. Second, our *ab initio* calculations show that the exciton excitation energies and also the onset of the continuum spectra decrease significantly with the decreasing diameter due to the curvature-induced orbital rehybridization in small-diameter zigzag BN nanotubes. This orbital rehybridization lowers the ionicity of the π^* bands by the formation of ringlike charge distribution inside the BN-NTs (Fig. 6), thus reducing the energy of the π^* bands and hence the band gap. The quasiparticle *GW* correction to the band gap is almost independent of the tube diameter.

Third, we find that the direction of the shift current in the BN-NTs is independent of the tube chirality $(n, 0)$ (or diameter), contrary to the simple detrimental rule of $\mathrm{sgn}(J_{\mathrm{shift}}) = \mathrm{mod}(n, 3)$ reported by previous model Hamiltonian studies [17,18]. Importantly, this implies that in a bundle of aligned zigzag BN-NTs, the contributions of the BN-NTs to the shift current would be additive rather than canceling each other as the simple rule suggests [17,18]. Finally, the effective 3D exciton shift current conductivity is nearly 10 times larger than the largest shift conductivity observed in ferroelectric semiconductors [61]. Furthermore, strongly bounded excitons with a large binding energy in the considered BN systems would impede thermal dissociation into free electron-hole pairs. All these properties would make the zigzag BN-NTs excellent candidates for experimentally studying the exciton shift current and also for promising applications in nanoscale optoelectronic devices.

ACKNOWLEDGMENTS

The authors gratefully acknowledge the support from the National Science and Technology Council and the National Center for Theoretical Sciences of the R.O.C. The authors also thank the National Center for High-performance Computing (NCHC) in Taiwan for providing computational and storage resources.

[1] W. Kraut and R. v. Baltz, Anomalous bulk photovoltaic effect in ferroelectrics: A quadratic response theory: A quadratic response theory, Phys. Rev. B **19**, 1548 (1979).

[2] B. I. Sturman and V. M. Fridkin, *The Photovoltaic and Photorefractive Effects in Noncentrosymmetric Materials* (Gordon and Breach, New York, 1992).

[3] C. Aversa and J. E. Sipe, Nonlinear optical susceptibilities of semiconductors: Results with a length-gauge analysis, Phys. Rev. B **52**, 14636 (1995).

[4] J. E. Sipe and A. I. Shkrebtii, Second-order optical response in semiconductors, Phys. Rev. B **61**, 5337 (2000).

[5] A. Bhatnagar, A. R. Chaudhuri, Y. H. Kim, D. Hesse, and M. Alexe, Role of domain walls in the abnormal photovoltaic effect in BiFeO$_3$, Nat. Commun. **4**, 2835 (2013).

[6] L. Z. Tan, F. Zheng, S. M. Young, F. Wang, S. Liu, and A. M. Rappe, Shift current bulk photovoltaic effect in polar materialshybrid and oxide perovskites and beyond, npj Comput. Mater. **2**, 16026 (2016).

[7] T. Morimoto and N. Nagaosa, Topological aspects of nonlinear excitonic processes in noncentrosymmetric crystals, Phys. Rev. B **94**, 035117 (2016).

[8] Y. H. Chan, D. Y. Qiu, F. H. da Jornada, and S. G. Louie, Giant exciton-enhanced shift currents and direct current conduction with subbandgap photo excitations produced by many-electron interactions, Proc. Natl. Acad. Sci. USA **118**, e1906938118 (2021).

[9] M. Sotome, M. Nakamura, T. Morimoto, Y. Zhang, G.-Y. Guo, M. Kawasaki, N. Nagaosa, Y. Tokura, and N. Ogawa, Terahertz emission spectroscopy of ultrafast exciton shift current in the noncentrosymmetric semiconductor CdS, Phys. Rev. B **103**, L241111 (2021).

[10] R. Saito, G. Dresselhaus, and M. S. Dresselhaus, *Physical Properties of Carbon Nanotubes* (Imperial College Press, London, 1998).

[11] G. Y. Guo, and J. C. Lin, Second-harmonic generation and linear electro-optical coefficients of BN nanotubes, Phys. Rev. B **72**, 075416 (2005).

[12] R. S. Lee, J. Gavillet, M. Lamy de la Chapelle, A. Loiseau, J. L. Cochon, D. Pigache, J. Thibault, and F. Willaime, Catalyst-free synthesis of boron nitride single-wall nanotubes with a preferred zig-zag configuration, Phys. Rev. B **64**, 121405(R) (2001).

[13] L. Wirtz, A. Marini, and A. Rubio, Excitons in Boron Nitride Nanotubes: Dimensionality Effects, Phys. Rev. Lett. **96**, 126104 (2006).

[14] C. H. Park, C. D. Spataru, and S. G. Louie, Excitons and Many-Electron Effects in the Optical Response of Single-Walled Boron Nitride Nanotubes, Phys. Rev. Lett. **96**, 126105 (2006).

[15] L. H. Li, Y. Chen, M. Y. Lin, A. M. Glushenkov, B. M. Cheng, and J. Yu, Single deep ultraviolet light emission from boron nitride nanotube film, Appl. Phys. Lett. **97**, 141104 (2010).

[16] J. Yu, D. Yu, Y. Chen, H. Chen, M. Y. Lin, B. M. Cheng, J. Li, and W. H. Duan, Narrowed bandgaps and stronger excitonic effects from small boron nitride nanotubes, Chem. Phys. Lett. **476**, 240 (2009).

[17] P. Král, E. J. Mele, and D. Tománek, Photogalvanic Effects in Heteropolar Nanotubes, Phys. Rev. Lett. **85**, 1512 (2000).

[18] S. Konabe, Exciton effect on shift current in single-walled boron-nitride nanotubes, Phys. Rev. B **103**, 075402 (2021).

[19] G. Y. Guo and J. C. Lin, Systematic *ab initio* study of the optical properties of BN nanotubes, Phys. Rev. B **71**, 165402 (2005).

[20] R. Fei, L. Z. Tan, and A. M. Rappe, Shift-current bulk photovoltaic effect influenced by quasiparticle and exciton, Phys. Rev. B **101**, 045104 (2020).

[21] A. Taghizadeh, and T. G. Pedersen, Gauge invariance of excitonic linear and nonlinear optical response, Phys. Rev. B **97**, 205432 (2018).

[22] R. W. Boyd, *Nonlinear Optics* (Elsevier, Amsterdam, 2003).

[23] G. Kresse and J. Hafner, Ab initio molecular dynamics for liquid metals, Phys. Rev. B **47**, 558 (1993).

[24] G. Kresse and J. Furthmuller, Efficient interactive schemes for ab initio total-energy calculations using a plane-wave basis set, Phys. Rev. B **54**, 11169 (1996).

[25] P. Giannozzi, O. Andreussi, T. Brumme, O. Bunau, M. B. Nardelli, M. Calandra, R. Car, C. Cavazzoni, D. Ceresoli, M. Cococcioni *et al.*, Advanced capabilities for materials modelling with QUANTUM ESPRESSO, J. Phys.: Condens. Matter **29**, 465901 (2017).

[26] D. R. Hamann, Optimized norm-conserving Vanderbilt pseudopotentials, Phys. Rev. B **88**, 085117 (2013).

[27] H. J. Monkhorst and J. D. Pack, Special points for Brillonin-zone integrations, Phys. Rev. B **13**, 5188 (1976).

[28] M. S. Hybertsen and S. G. Louie, Electron correlation in semiconductors and insulators: Band gaps and quasiparticle energies, Phys. Rev. B **34**, 5390 (1986).

[29] M. Rohlfing and S. G. Louie, Electron-hole excitations and optical spectra from first principles, Phys. Rev. B **62**, 4927 (2000).

[30] J. Deslippe, G. Samsonidze, D. A. Strubbe, M. Jain, M. L. Cohen, and S. G. Louie, BerkeleyGW: A massively parallel computer package for the calculation of the quasiparticle and optical properties of materials and nanostructures, Comput. Phys. Commun. **183**, 1269 (2012).

[31] F. H. da Jornada, D. Y. Qiu, and S. G. Louie, Nonuniform sampling schemes of the Brillouin zone for many-electron perturbation-theory calculations in reduced dimensionality, Phys. Rev. B **95**, 035109 (2017).

[32] S. Ismail-Beigi, Truncation of periodic image interactions for confined systems, Phys. Rev. B **73**, 233103 (2006).

[33] J. Ibañez-Azpiroz, S. S. Tsirkin, and I. Souza, Ab initio calculation of the shift photocurrent by Wannier interpolation, Phys. Rev. B **97**, 245143 (2018).

[34] I. Souza, J. iguez, and D. Vanderbilt, Dynamics of Berry-phase polarization in time-dependent electric fields, Phys. Rev. B **69**, 085106 (2004).

[35] K. S. Virk and J. E. Sipe, Semiconductor optics in length gauge: A general numerical approach, Phys. Rev. B **76**, 035213 (2007).

[36] F. Zhang, C. S. Ong, J. W. Ruan, M. Wu, X. Q. Shi, Z. K. Tang, and S. G. Louie, Intervalley Excitonic Hybridization, Optical Selection Rules, and Imperfect Circular Dichroism in Monolayer h-BN, Phys. Rev. Lett. **128**, 047402 (2022).

[37] H. Şahin, S. Cahangirov, M. Topsakal, E. Bekaroglu, E. Akturk, R. T. Senger, and S. Ciraci, Monolayer honeycomb structures of group-IV elements and III-V binary compounds: First-principles calculations, Phys. Rev. B **80**, 155453 (2009).

[38] F. A. Rasmussen, P. S. Schmidt, K. T. Winther, and K. S. Thygesen, Efficient many-body calculations for two-dimensional materials using exact limits for the screened

potential: Band gaps of MoS_2, h-BN, and phosphorene, Phys. Rev. B **94**, 155406 (2016).

[39] I. Guilhon, M. Marques, L. K. Teles, M. Palummo, O. Pulci, Silvana Botti, and F. Bechstedt, Out-of-plane excitons in two-dimensional crystals, Phys. Rev. B **99**, 161201(R) (2019).

[40] H. Mishra and S. Bhattacharya, Giant exciton-phonon coupling and zero-point renormalization in hexagonal monolayer boron nitride, Phys. Rev. B **99**, 165201 (2019).

[41] F. Ferreira, A. J. Chaves, N. M. R. Peres, and R. M. Ribeiro, Excitons in hexagonal boron nitride single-layer: a new platform for polaritonics in the ultraviolet, J. Opt. Soc. Am. B **36**, 674 (2019).

[42] T. Galvani, F. Palean, H. P. C. Miranda, A. Molina-Sanchez, L. Wirtz, S. Latil, H. Amara, and F. Ducastelle, Excitons in boron nitride single layer, Phys. Rev. B **94**, 125303 (2016).

[43] H. C. Hsueh, G. Y. Guo, and S. G. Louie, Excitonic effects in the optical properties of a SiC sheet and nanotubes, Phys. Rev. B **84**, 085404 (2011).

[44] A. Nagashima, N. Tejima, Y. Gamou, T. Kawai, and C. Oshima, Electronic dispersion relations of monolayer hexagonal boron nitride formed on the Ni(111) surface, Phys. Rev. B **51**, 4606 (1995).

[45] C. Elias, P. Valvin, T. Pelini, A. Summerfield, C. J. Mellor, T. S. Cheng, L. Eaves, C. T. Foxon, P. H. Beton, S. V. Novikov, B. Gil, and G. Cassabois, Direct band-gap crossover in epitaxial monolayer boron nitride, Nat. Commun. **10**, 2639 (2019).

[46] X. Li, H. Qiu, X. F. Liu, J. Yin, and W. Guo, Wettability of Supported Monolayer Hexagonal Boron Nitride in Air, Adv. Funct. Mater. **27**, 1603181 (2017).

[47] R. J. P. Román, F. J. R. Costa Costa, A. Zobelli, C. Elias, P. Valvin, G. Cassabois, B. Gil, A. Summerfield, T. S. Cheng, C. J. Mellor, P. H. Beton, S. V. Novikov, and L. F. Zagonel, Band gap measurements of monolayer h-BN and insights into carbon-related point defects, 2D Mater. **8**, 044001 (2021).

[48] C. Thomsen, S. Reich, and J. Maultzsch, *Carbon Nanotubes: Basic Concepts and Physical Properties* (Wiley, Weinheim, 2004).

[49] X. Blase, A. Rubio, S. G. Louie, and M. L. Cohen, Stability and band gap constancy of boron nitride nanotubes, Europhys. Lett. **28**, 335 (1994).

[50] A. Rubio, J. L. Corkill, and M. L. Cohen, Theory of graphitic boron nitride nanotubes, Phys. Rev. B **49**, 5081 (1994).

[51] R. Arenal, O. Stéphan, M. Kociak, D. Taverna, A. Loiseau, and C. Colliex, Electron Energy Loss Spectroscopy Measurement of the Optical Gaps on Individual Boron Nitride Single-Walled and Multiwalled Nanotubes, Phys. Rev. Lett. **95**, 127601 (2005).

[52] G. G. Fuentes, E. Borowiak-Palen, T. Pichler, X. Liu, A. Graff, G. Behr, R. J. Kalenczuk, M. Knupfer, and J. Fink, Electronic structure of multiwall boron nitride nanotubes, Phys. Rev. B **67**, 035429 (2003).

[53] D. Y. Qiu, F. H. da Jornada, and S. G. Louie, Screening and many-body effects in two-dimensional crystals: Monolayer MoS_2, Phys. Rev. B **93**, 235435 (2016).

[54] B. Arnaud, S. Lebegue, P. Rabiller, and M. Alouani, Huge Excitonic Effects in Layered Hexagonal Boron Nitride, Phys. Rev. Lett. **96**, 026402 (2006)

[55] A. R. Beal, J. C. Knights, and W. Y. Liang, Transmission spectra of some transition metal dichalcogenides. II. Group VIA: Trigonal prismatic coordination, J. Phys. C: Solid State Phys. **5**, 3540 (1972).

[56] A. Strasser, H. Wang, and X. Qian, Nonlinear optical and photocurrent responses in janus MoSSe monolayer and MoS2-MoSSe van der waals heterostructure, Nano Lett. **22**, 4145 (2022).

[57] E. J. Mele and P. Král, Electric Polarization of Heteropolar Nanotubes as a Geometric Phase, Phys. Rev. Lett. **88**, 056803 (2002).

[58] B. M. Fregoso, T. Morimoto, and J. E. Moore, Quantitative relationship between polarization differences and the zero-averaged shift photocurrent, Phys. Rev. B **96**, 075421 (2017)

[59] S. M. Nakhmanson, A. Calzolari, V. Meunier, J. Bernholc, and M. B. Nardelli, Spontaneous polarization and piezoelectricity in boron nitride nanotubes, Phys. Rev. B **67**, 235406 (2003).

[60] W. T. H. Koch, R. Munser, W. Ruppel, and P. Wurfel, Anomalous photovoltage in $BaTiO_3$, Ferroelectrics **13**, 305 (1976)

[61] M. Sotome, M. Nakamura, J. Fujioka, M. Ogino, Y. Kaneko, T. Morimoto, Y. Zhang, M. Kawasaki, N. Nagaosa, Y. Tokura, and N. Ogawa, Spectral dynamics of shift current in ferroelectric semiconductor SbSI, Proc. Natl. Acad. Sci. USA **116**, 1929 (2019).

[62] B. Sturman, Ballistic and shift currents in the bulk photovoltaic effect theory, Physics-Uspekhi **63**, 407 (2020).

[63] T. Morimoto and N. Nagaosa, Nonreciprocal current from electron interactions in noncentrosymmetric crystals: Roles of time reversal symmetry and dissipation, Sci. Rep. **8**, 2973 (2018).

[64] T. Morimoto, S. Kitamura, and N. Nagaosa, Geometric aspects of nonlinear and nonequilibrium phenomena, J. Phys. Soc. Jpn. **92**, 072001 (2023).